



## Experimental study of liquid drop impact onto a powder surface

J.O. Marston<sup>a,b,\*</sup>, S.T. Thoroddsen<sup>b</sup>, W.K. Ng<sup>a</sup>, R.B.H. Tan<sup>a,c</sup>

<sup>a</sup> Institute of Chemical and Engineering Sciences, 1 Pesek Road, Jurong Island, Singapore 627833, Singapore

<sup>b</sup> Division of Physical Sciences and Engineering, King Abdullah University of Science and Technology, Thuwal 23955-6900, Saudi Arabia

<sup>c</sup> Department of Chemical and Biomolecular Engineering, National University of Singapore, 4 Engineering Drive 4, Singapore 117576, Singapore

### ARTICLE INFO

#### Article history:

Received 27 January 2010

Received in revised form 4 May 2010

Accepted 8 May 2010

Available online 26 May 2010

#### Keywords:

Drop impact

High-speed imaging

Granulation

Nucleation

### ABSTRACT

The initial dynamics of liquid drop impact onto powder surfaces is studied experimentally using high-speed photography. For a range of bed packing fractions,  $\phi$ , liquid physical properties and impact velocities,  $u_i$ , we observe a variety of phenomena that can be representative of a hydrophobic surface, a rough surface or a porous medium. The solids packing fraction in the bed,  $0.38 \leq \phi \leq 0.65$ , and the impact Weber number,  $3.5 \leq We = \rho D u_i^2 / \sigma \leq 750$ , (where  $\rho$ ,  $D$  and  $\sigma$  are the drop density, diameter and surface tension respectively) are shown to be the critical parameters governing the outcome of an impact. For high packing fractions,  $\phi \geq 0.5$ , we show that the observed spreading, rebound and splashing can be broadly characterised in terms of the Weber number while for looser packing fractions,  $\phi \leq 0.5$ , we observe powder ejectas and provide a qualitative description of the granule nucleation at the centre of the impact sites.

© 2010 Elsevier B.V. All rights reserved.

### 1. Introduction

Drop impact onto both rigid solid and divided solid surfaces is of great importance to industry. In the former, research is motivated by processes such as spray-coating and cooling whereas in the latter, wet granulation is one example of a key driver.

The large number of physical and material parameters and the importance of this topic are reflected by the large number of papers found in the literature dedicated to the topic of drop impact. These previous efforts have been experimental, theoretical and numerical in nature (see Yarin [1] for a review of drop impact onto solid and liquid target surfaces).

The phenomena of drop impact onto powders, however, has received little attention, despite its significance, particularly to the process of granulation where the impact of binder droplets onto a particulate surface constitutes the first stage of liquid–solid interaction. The impact itself is classified as step two in the nucleation process where the five steps are droplet formation, droplet impact and breakage, droplet coalescence, drop penetration and mechanical dispersion as described by Hapgood et al. [2]. This is a key stage as the wetting and nucleation of the powder effectively determines the granule size distribution and other downstream processes such as attrition and drying [3]. Previous studies [4,5] essentially quantify the wetting regime by means of the penetration times of drops into the powder beds, but do not inspect the influence of the impact conditions.

Liquid droplet motion throughout a powder bed in a high-shear granulator was studied by Chouk et al. [6] with the use of PIV (Particle Image Velocimetry) analysis and droplet motion onto partially wetted surfaces has been considered by Hapgood et al. [7]. However neither study incorporate the influence of the impact conditions nor the initial impact dynamics.

Recent research by Hapgood and Khanmohammadi [8] has shown that it is possible to exploit ideas of wetting dynamics in the interaction between liquids and fine powders, showing the potential of producing custom design granules using powders as a means to store liquid via encapsulation [9]. In these experiments, the liquid drops were deposited onto hydrophobic powder and although some trials were performed at higher impact velocities, showing that the impact kinetic energy has a significant effect on the initial powder coverage of the drop, this effect was not quantified. The stability and survival rates of these marbles and their ability to form hollow granules was examined by Eshtiaghi et al. [10]. Aussillous and Quere [11] provide an interesting review of the properties including, for example, the robustness and mobility of these encapsulations, also referred to as ‘liquid marbles’.

Knowledge of the behaviour of the drop during the initial stages and, in particular, droplet breakage regimes and prediction of satellite (secondary) droplet generation is crucial in order to predict granule nucleus size distributions. Hence these features are key focal points in this work. With the use of high-speed photography at typical frame rates of 15,000 fps, we observe the initial impact dynamics, i.e.  $t < 50$  ms, of roughly spherical liquid drops, i.e.  $Bo = \rho g D^2 / \sigma \sim 1$ , onto powder beds. The Bond number,  $Bo$ , represents the ratio gravitational to surface tension forces. By primarily focusing on a single particle size distribution, we examine the influence of impact velocity, liquid

\* Corresponding author. Division of Physical Sciences and Engineering, King Abdullah University of Science and Technology, Thuwal 23955-6900, Saudi Arabia.  
E-mail address: [jeremy.marston@kaust.edu.sa](mailto:jeremy.marston@kaust.edu.sa) (J.O. Marston).

**Table 1**Characteristic measurements from particle size analysis. All values stated in  $\mu\text{m}$ .

Supplier-stated range	$d_{10}$	$d_{50}$	$d_{90}$	$d_{3,2}$	$d_{4,3}$
0–53	18.96	29.76	45.92	27.9	31.35

**Table 2**Physical properties of liquids used. The stated values of the Ohnesorge number,  $Oh$ , and Bond number,  $Bo$  are based on  $D = 1.8\text{--}2.4\text{ mm}$ , depending on the liquid.

Drop liquid	$D$ (mm)	$\rho$ ( $\text{kg m}^{-3}$ )	$\mu$ ( $\text{mPa s}$ )	$\sigma$ ( $\text{N m}^{-1}$ )	$Oh$	$Bo$
Water	2.2	996	1.004	0.072	0.0027	0.64
Ethanol	1.8	789	1.19	0.0232	0.0066	1.08
Ethanol/water (50/50)	1.9	900	1.1	0.0279	0.005	1.14
Acetone	1.8	791	0.306	0.0237	0.0016	1.12
Glycerol	2.3	1260	$\sim 1000$	0.065	2.3	1
Glycerol/water (50/50)	2.4	1100	8.4	0.0674	0.0199	0.92

physical properties and bed packing fraction. Here, we do not observe full liquid marble formation as described by Aussillous and Quere [11] and Hapgood and Khanmohammadi [8], rather a transition of behaviour from spread-retraction to full rebound (with partial powder coating) to prompt splash regimes, all dependent on the solids packing and the impact Weber number. The rich variety of

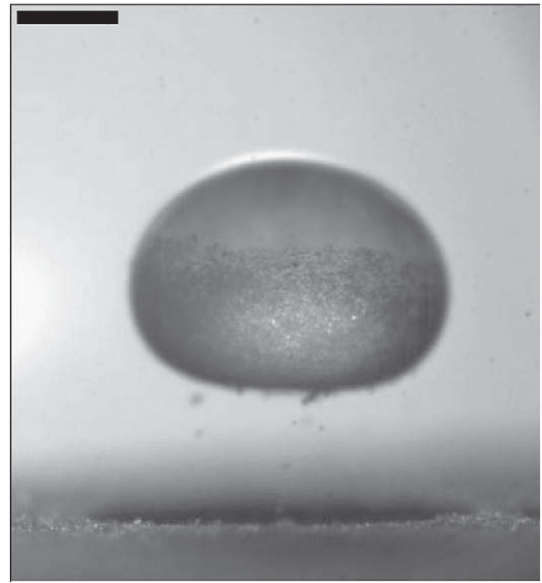


**Fig. 2.** Snapshot of a 2 mm water drop during rebound with partial powder coating. The frame shown is taken at 15 ms after impact. The impact velocity,  $u_i = 0.50\text{ m/s}$  and the solids packing in the base,  $\phi \sim 0.62$ .  $We = 6.9$ ,  $Oh = 0.00272$ ,  $Bo = 0.64$ . The scale bar is 1 mm. See also the supplementary movie for this Figure.

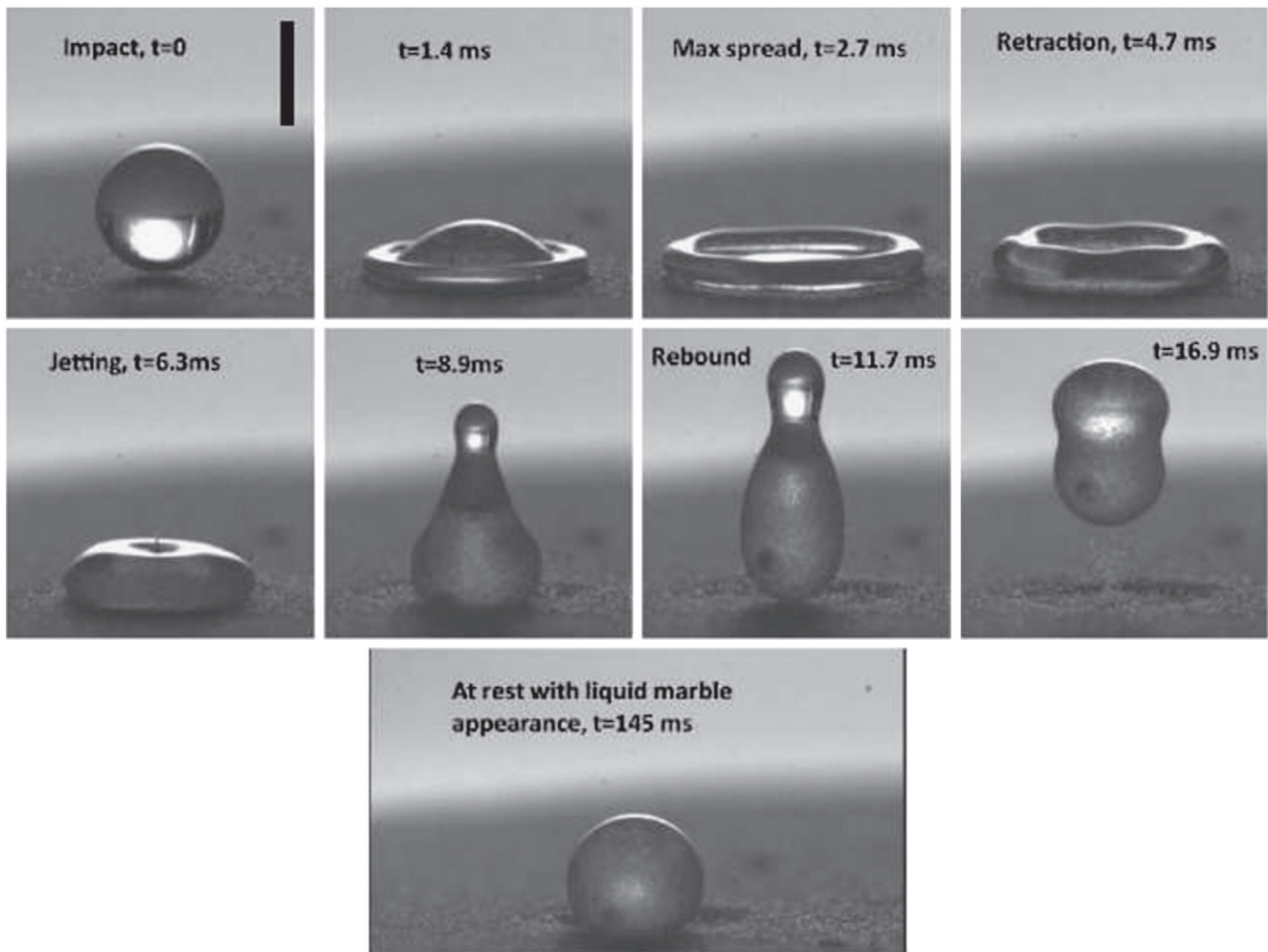


**Fig. 1.** Sequence of events for the impact of a  $D = 2.4\text{ mm}$  50% glycerol drop onto a base of  $31\text{ }\mu\text{m}$  glass beads. The impact velocity,  $u_i = 1.12\text{ m/s}$  and the solids packing in the base,  $\phi \sim 0.58$ .  $We = 49$ ,  $Oh = 0.0282$ ,  $Bo = 0.92$ . Note the emergence of a fine vertical jet from the centre of the retracting drop at 6.3 ms from impact. The scale bar is 2 mm.

dynamics observed and criteria for regime transitions are described. We note distinct quantitative and qualitative differences for high (e.g.  $\phi \geq 0.5$ ) and low (e.g.  $\phi \leq 0.5$ ) solid packing fractions.

## 2. Materials and methods

In order to quantify the effect of the impact conditions and bed packing fraction, we focus mainly on one base particle size distribution. The particles used in the experiments were glass beads and were untreated, i.e. 'as supplied' by the manufacturer (Pan Abrasives Pte Ltd, Singapore) with no washing or treatment prior to use. The size range stated by the supplier was  $0 < d_b < 53 \mu\text{m}$ . Samples of these beads were subjected to particle size analysis by a wet (sample dispersed in water) laser diffraction method on a Malvern Mastersizer 2000. The results of this analysis are shown in Table 1.

For convenience, throughout the remainder of this paper, we refer to the beads using the equivalent volume mean measurement  $d_{4,3} = 31 \mu\text{m}$  as the characteristic particle size.

The powder beds were prepared by packing the beads into small cylindrical plexi-glass containers (Depth = 19 mm, Diameter = 25 mm) with light compression and then scraping the surface several times with a microscope slide to ensure a uniform, level

surface. Using this method, the packing was reproducible for successive repeat experiments. The packing fraction of the solid,  $\phi$ , was determined from the difference in mass between an empty and a filled container. Using this method, the resulting packing fractions were in the range  $0.48 \leq \phi \leq 0.66$ . Looser packings,  $0.38 \leq \phi \leq 0.45$ , were produced by shaking beads into the container and not using compression, just levelling of the surface.

The liquids used in this study along with their physical properties are listed in Table 2. To ensure consistency, all the experiments, as well as physical property measurements, were performed in air-conditioned laboratories with ambient temperature of 23 °C.

These liquids were selected to achieve a range of viscosities and surface tensions in order to investigate a range of the characteristic dimensionless numbers for this problem – namely the Bond number, the Weber number and the Ohnesorge number:

$$Bo = \frac{\rho g D^2}{\sigma}, \quad We = \frac{\rho D u_i^2}{\sigma}, \quad Oh = \frac{\mu}{\sqrt{\rho \sigma D}},$$

where  $\rho$ ,  $\mu$  and  $\sigma$  are the drop density, dynamic viscosity and surface tension respectively,  $g$  is acceleration due to gravity and

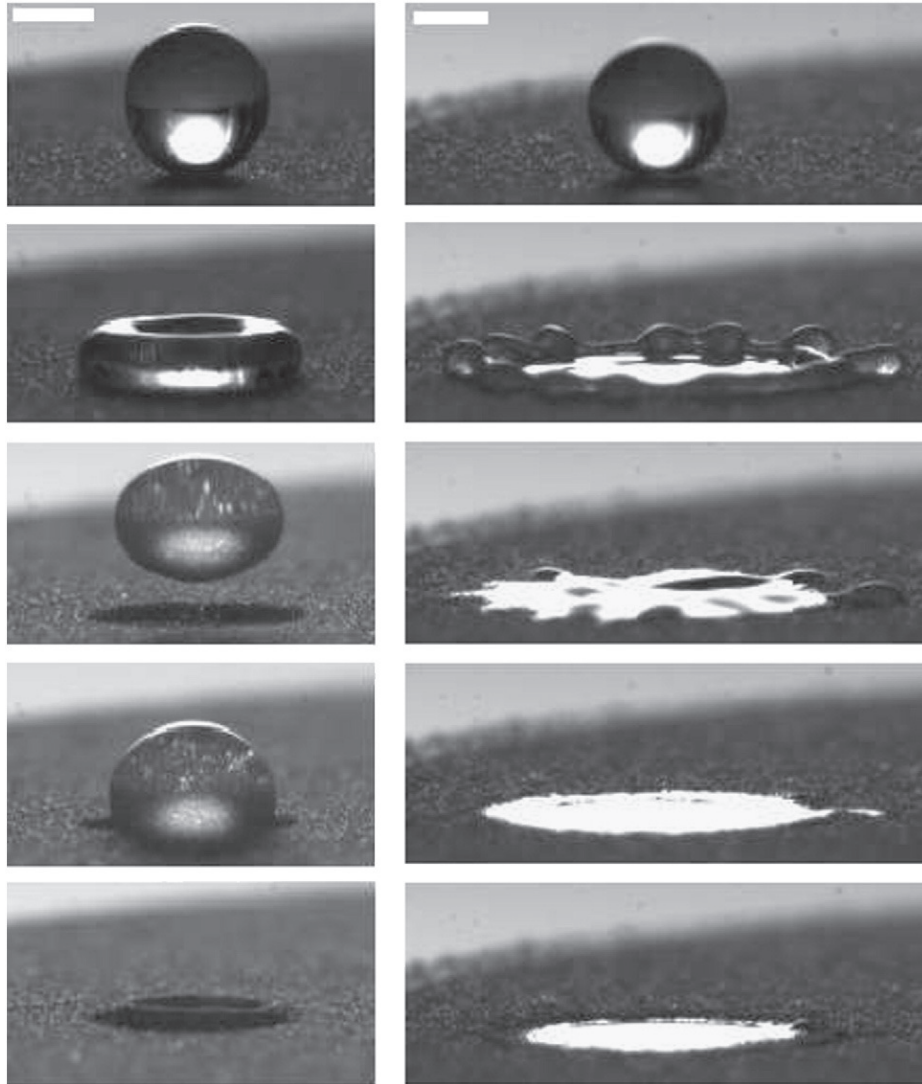


**Fig. 3.** Example sequences of events for the impact a  $D = 1.8 \text{ mm}$  ethanol drop onto a base of  $31 \mu\text{m}$  glass beads. Left panels:  $u_i = 0.38 \text{ m/s}$ ,  $\phi \sim 0.55$ ,  $We = 8.8$ ,  $Oh = 0.0066$ ,  $Bo = 1.08$  with frames shown taken at 0, 4.8, 18.6, 55.7 ms from impact and the final frame is taken approximately 1 min after impact. Right panels:  $u_i = 1.49 \text{ m/s}$ ,  $\phi \sim 0.52$ ,  $We = 136$ ,  $Oh = 0.0066$ ,  $Bo = 1.08$  with frames shown taken at 0, 3, 6.8, 14.5 and 24.7 ms from impact. The scale bars are 1 mm. See also the supplementary movies for this Figure.

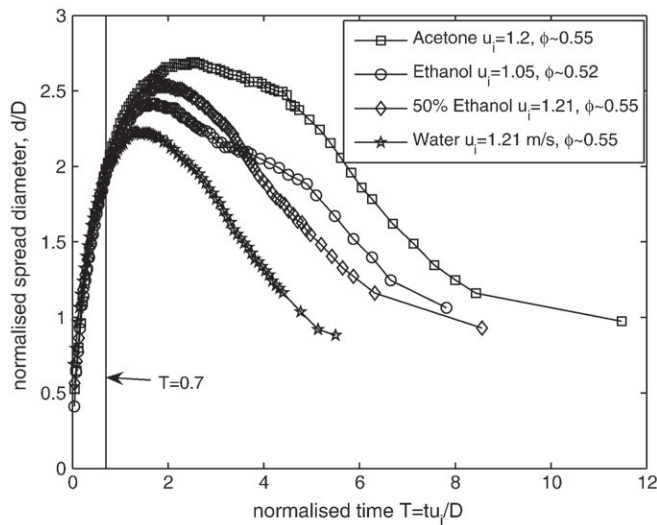


**Fig. 4.** Spread diameter of impacting drops as a function of time. The spread diameter is normalised by the initial drop diameter and the time is normalised by the natural timescale  $D/u_i$ . Various low viscosity liquids are shown at similar impact velocities and solids packing fraction; acetone ( $Oh=0.0016$ ,  $Bo=1.12$ ,  $We=88$ ), ethanol ( $Oh=0.0066$ ,  $Bo=1.08$ ,  $We=66$ ), 50% ethanol ( $Oh=0.005$ ,  $Bo=1.14$ ,  $We=85$ ), water ( $Oh=0.0027$ ,  $Bo=0.64$ ,  $We=44$ ).

$u_i = \sqrt{2g(h_r - D)}$  is the impact velocity. Drops were released to fall freely from various heights from  $h_r \sim 1$  cm (near-surface deposition) to  $h_r \sim 1$  m producing a wide range of impact velocities. As the drop release height is increased, the drop deforms during free-fall due to air resistance, however, analysis of the drops shows that this 'flattening' results in less than 7% distortion of the drop.

The drops were produced using a 10  $\mu$ l Hamilton syringe with a cemented 26 Gauge needle for low viscosity liquids or a 1 ml syringe with a 23 Gauge needle for higher viscosity liquids. As such, the drop diameters were  $1.8 \leq D \leq 2.4$  mm (measured directly from the video frames) depending on the physical properties of the liquid resulting in Bond numbers  $0.64 < Bo < 1.14$ .

The impact events were observed with a high-speed video camera (Photron Fastcam SA-1) with a typical frame rate of 15,000 fps and

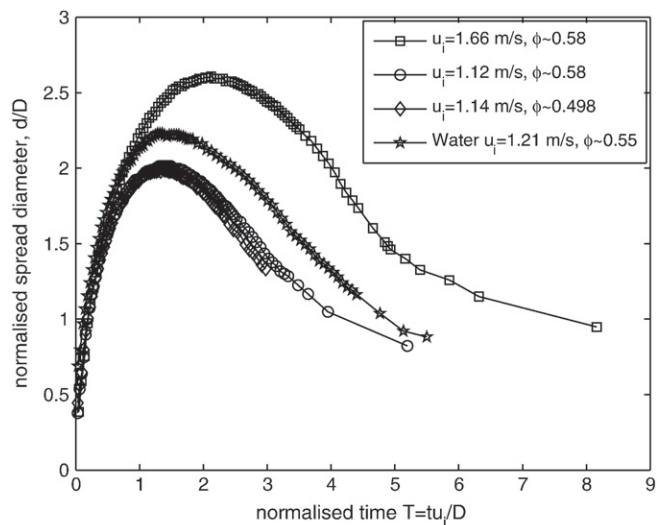


**Fig. 5.** Spread diameter of impacting drops as a function of time. The spread diameter is normalised by the initial drop diameter and the time is normalised by the natural timescale  $D/u_i$ . Curves shown are for various impact conditions of 50% glycerol drops ( $Oh=0.019$ ,  $Bo=0.92$ ) at  $We=108$ , 49 and 51. Also shown is the data for water from Fig. 4.

corresponding pixel resolution of  $960 \times 416$  pixels. In some instances, however, frame rates up to 30,000 fps were used. The video clips were saved directly to a PC for subsequent analysis.

Several repeat trials were performed for each individual release height – liquid – bed packing combination. Due to the heterogeneous nature of the target surface for these experiments, some minor discrepancies were noted between individual trials, however, the overall qualitative and quantitative observations were consistent.

### 3. Results and discussion

Some typical examples of the impact process are shown in Figs. 1–3 for 50% glycerol, water and ethanol respectively impacting densely packed beds with  $\phi=0.58$ , 0.62 and 0.55 respectively. In all of these sequences, the base is the 31  $\mu$ m powder and the frames shown are from video clips taken at 15,000 fps.

In Fig. 1, for 50% glycerol ( $\mu=8.4$  mPa s,  $u_i=1.12$  m/s,  $We=49$ ), the impact appears to show characteristic behaviour of a liquid drop impacting a hydrophobic surface [12–14] where the drop deforms to a

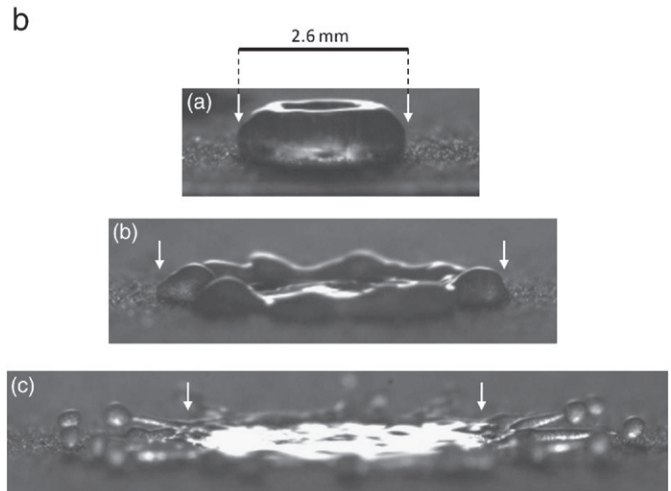
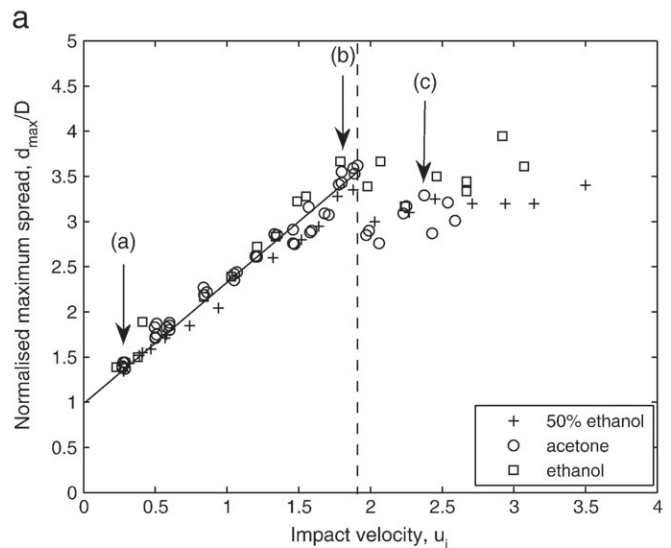


**Fig. 6.** (a) Maximum spread diameter (normalised by initial drop diameter) plotted against impact velocity,  $u_i$ , for liquids with  $Bo > 1$ . The solids packing in the base varied slightly between repeat trials in the range  $0.51 < \phi < 0.56$ . The dashed line marks the onset of satellite drop detachment from the fingers. (b) Images of acetone drops at maximum spread in different regimes, indicated by arrows on the plot in part (a).

maximum extent at  $t=2.7$  ms at which point the drop has assumed a toroidal shape. Following this, the drop then retracts and the collapse of the central cavity at the apex of the drop results in the formation of a singular jet at  $t=6.3$  ms. The drop continues to deform in the vertical axis forming a prolate shape, eventually lifting completely off the surface at  $t=11.7$  ms. During the spreading phase, particles from the powder bed adhere to the underside of the drop, providing the drop with a semi-coating of powder. This coating is seen more easily at higher magnification in Fig. 2 for the water drop. The clear demarcation represents the extent of the contact area of the drop during the spreading phase. However, since the surface area of the flattened shape at maximum deformation is greater than that of the sphere with the same volume, a greater surface area will be covered by particles once the drop resumes its spherical shape. Finally, the drop comes to rest on the powder bed and may remain in its spherical form for a short time before draining into the bed.

It is precisely this powder coating attained during impact which acts to delay the wetting of the powder bed by providing the drop with a surface barrier that temporarily maintains the Laplace pressure of the drop before the onset of wetting occurs. The fact that the

powder in the vicinity is compressed during impact is also likely to contribute to this delay.

To highlight the extent to which the powder coating acts, Fig. 3 shows two impact sequences for ethanol drops at different impact velocities. The left panel of images shows a typically low impact velocity,  $u_i=0.38$  m/s, with a packing fraction of  $\phi=0.55$  whilst the right panel shows a higher impact velocity of  $u_i=1.49$  m/s with a packing fraction of  $\phi=0.52$ . In the first case, the conditions are favourable for rebound with base particles coating the lower hemisphere of the drop which has come to rest in the impact crater at  $t\sim 55$  ms and does not fully drain until approximately 1 min after impact. In contrast, the drop impacting at  $u_i=1.49$  m/s has spread on the surface and undergoes fast penetration into the bed which is nearly complete at  $t=24.7$  ms (final image). These two cases clearly show the delay in the onset of wetting induced for different impact conditions. In the former, the powder coating and higher packing fraction essentially provides the drop with a contact angle much higher than  $90^\circ$  whereas in the latter, the contact angle is much lower than  $90^\circ$  so that penetration by capillarity is relatively fast [7].

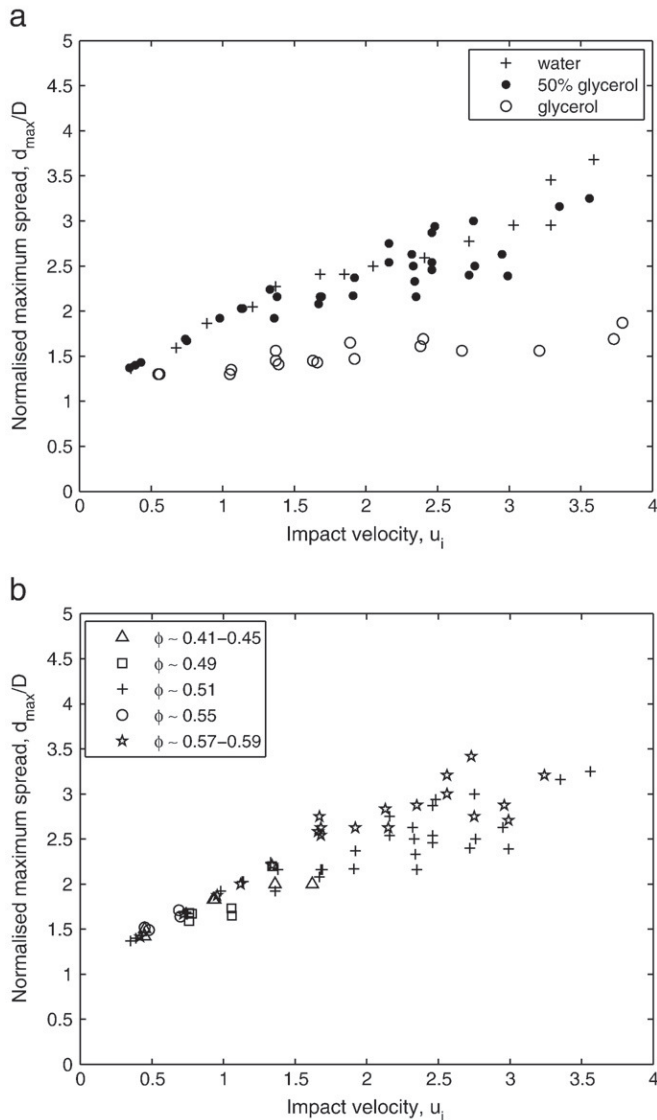


Fig. 7. Maximum spread diameter (normalised by initial drop diameter) plotted against impact velocity,  $u_i$ , for (a) liquids for  $Bo \leq 1$  with  $0.51 < \phi < 0.55$  and (b) 50% glycerol for various packing fractions.

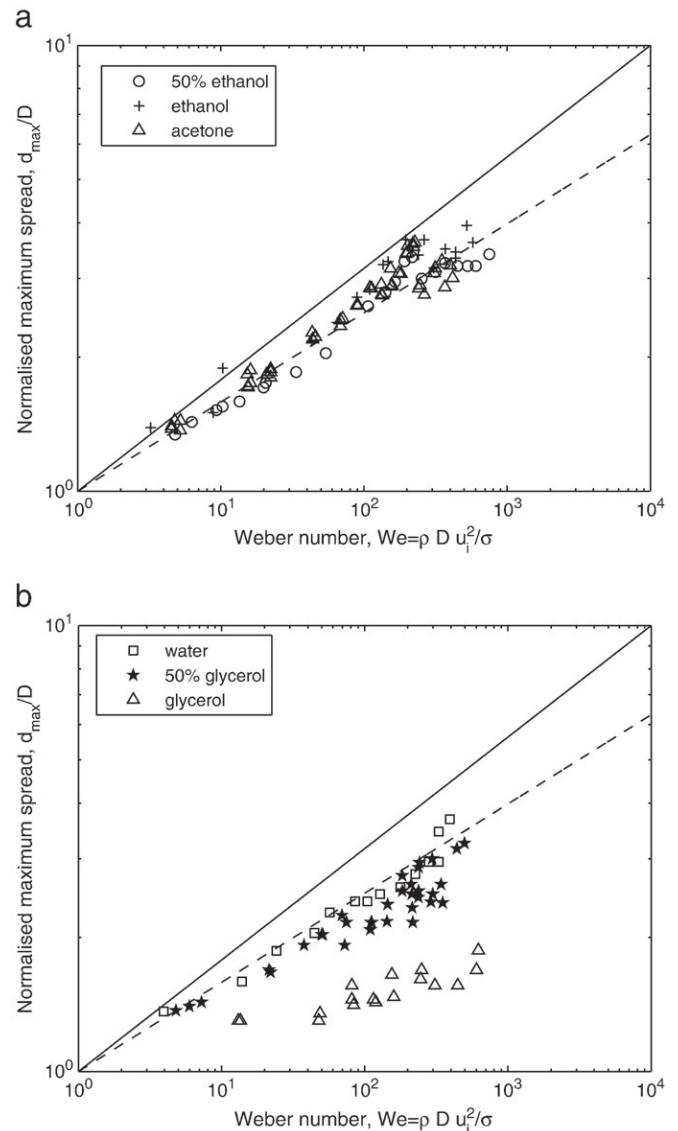
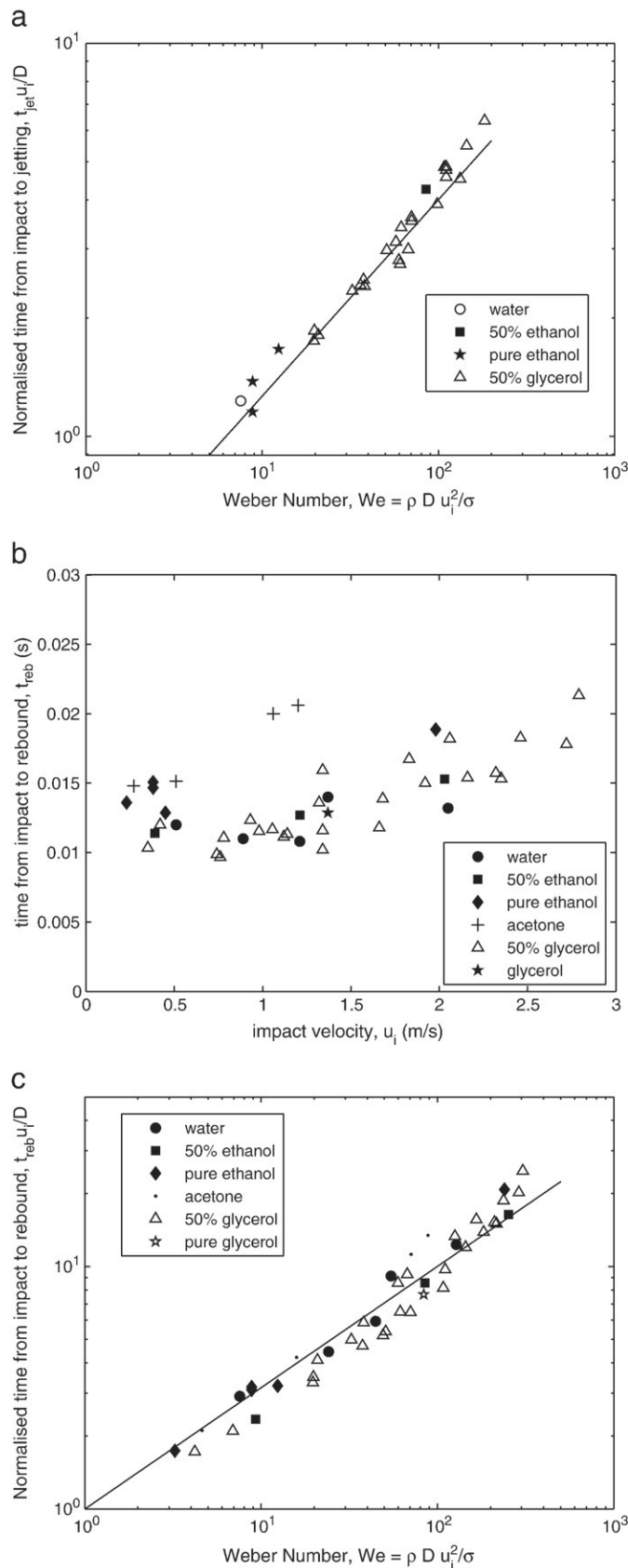
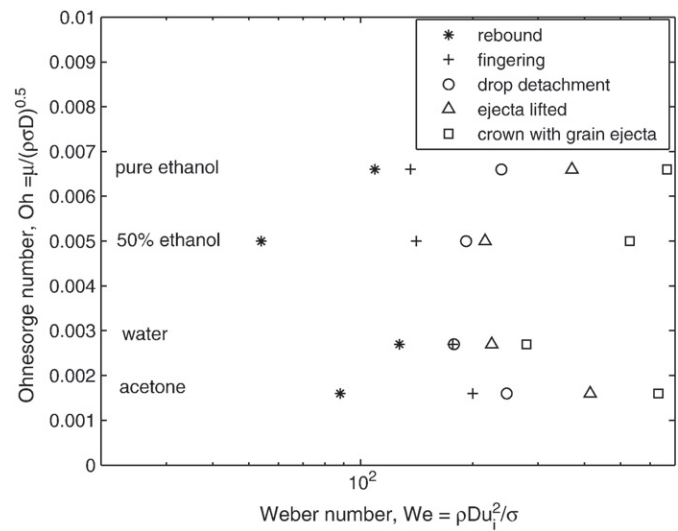


Fig. 8. Maximum spread diameter (normalised by initial drop diameter) plotted against impact Weber number,  $\rho D u_i^2 / \sigma$  for (a)  $Bo > 1$  and (b)  $Bo \leq 1$  all liquids. The solid line indicates a slope of 1/4 and the dashed line 1/5.



**Fig. 9.** (a) Time from impact to the emergence of the singular jet, plotted against the Weber number (solid line indicates a slope of 1/2); (b) Contact time from impact to rebound from the surface, plotted against the impact velocity; (c) Time from impact to rebound plotted against the Weber number (solid line indicates a slope of 1/2). All impacts were for solids packings in the range  $0.51 < \phi < 0.56$ .



**Fig. 10.** Map of the transitions between different regimes for low viscosity liquids plotted in the  $Oh$ - $We$  plane. Note this plot is for solids packings  $0.51 < \phi < 0.55$ .

### 3.1. Spreading dynamics – dense packings

Figs. 4 and 5 show examples of the time evolution of the diameter at the base of the drop as it deforms during impact. In these Figures, the spread diameter,  $d$ , has been normalised with respect to the initial drop diameter,  $D$  and the time (measured from impact) has been normalised with respect to the naturally occurring timescale,  $D/u_i$ . The uncertainty of the impact time is confined to within one frame of the video sequence so that the maximum error in the location of the reference time  $T = 0$  is  $67 \mu\text{s}$ .

Fig. 4 shows example spreading for low viscosity liquids (acetone, ethanol and 50% ethanol) with water as a reference case (note only the initial spreading and retraction phases are shown). The curves are shown to be indistinguishable for  $T \leq 0.7$ , which is understood to be the inertial regime during which viscous and surface tension forces are negligible [15]. The maximum spreading (i.e. the local maxima on each curve) is found to slightly increase with the Weber number from  $d_{max}/D = 2.23$  at  $T = 1.28$  for water ( $We = 44$ ) to  $d_{max}/D = 2.69$  at

**Table 3**

Qualitative observations of 50% glycerol drop impacts onto various solid packing.

$h_r$ (cm)	$u_i$ (m/s)	$\phi = 0.41-0.45$	$\phi = 0.48-0.51$	$\phi = 0.57-0.59$
1	0.45	Rebound, pinned due to penetration	Rebound, 1/2 marble	Rebound, 1/2 marble
3	0.71			Rebound, pinned at base
5	0.93	Full rebound w/ jetting		Jetting
7	1.14			Full rebound w/ jetting
10	1.35	Rebound w/ jetting and powder ejecta		
15	1.67		Powder ejecta, rim undulations	Jetting ends
20	1.95			Fingering, recoil
35	2.46		Fingering	Horizontal splash
40	2.7		Drops detach	Slight powder ejecta
50	2.9		Strong powder ejecta	Crown, powder ejecta
60	3.19	Fingering		
80	3.65	Large powder ejection and drop penetration		

$T=2.48$  for acetone ( $We = 88$ ). The faster retraction rate for water is to be expected as surface tension forces become important after the maximum spread has been reached.

Fig. 5 shows an earlier decoupling, at  $T \sim 0.3$ , for the spreading of the higher viscosity 50% glycerol drops. Note that the effect of impact velocity is evident in this Figure; this is clear when comparing the data for  $u_i = 1.66$  m/s ( $d_{max}/D = 2.61$  at  $T = 2.12$ ) against the data for  $u_i = 1.12$  m/s ( $d_{max}/D = 2.01$  at  $T = 1.31$ ). The effect of the solids fraction in the target surface also appears negligible under these conditions – as can be seen in the two bottom curves where  $\phi \sim 0.58$  and  $0.498$  respectively with no significant discrepancies between the

two data sets. For even higher impact velocities, however, the effect of the solids packing becomes substantial – this is discussed later. The same case for water from Fig. 4 is replotted here for reference.

By examining data for  $d_{max}$  against  $u_i$ , we can broadly classify the results into two separate cases – namely –  $Bo > 1$  (Fig. 6(a) and (b) and Fig. 8(a)) and  $Bo \leq 1$  (Fig. 7(a) and (b) and Fig. 8(b)). These classifications arise due to the fact that for  $Bo > 1$ , the drops are larger than the capillary length so different shapes are expected at maximum deformation during impact [3]. In Fig. 6(a), the data for drop impacts with  $Bo > 1$  is shown over a range of impact velocities,  $0.23$  m/s  $\leq u_i \leq 3.5$  m/s, showing a clear trend for all drops up to  $u_i \sim 1.9$  m/s beyond which the fingering

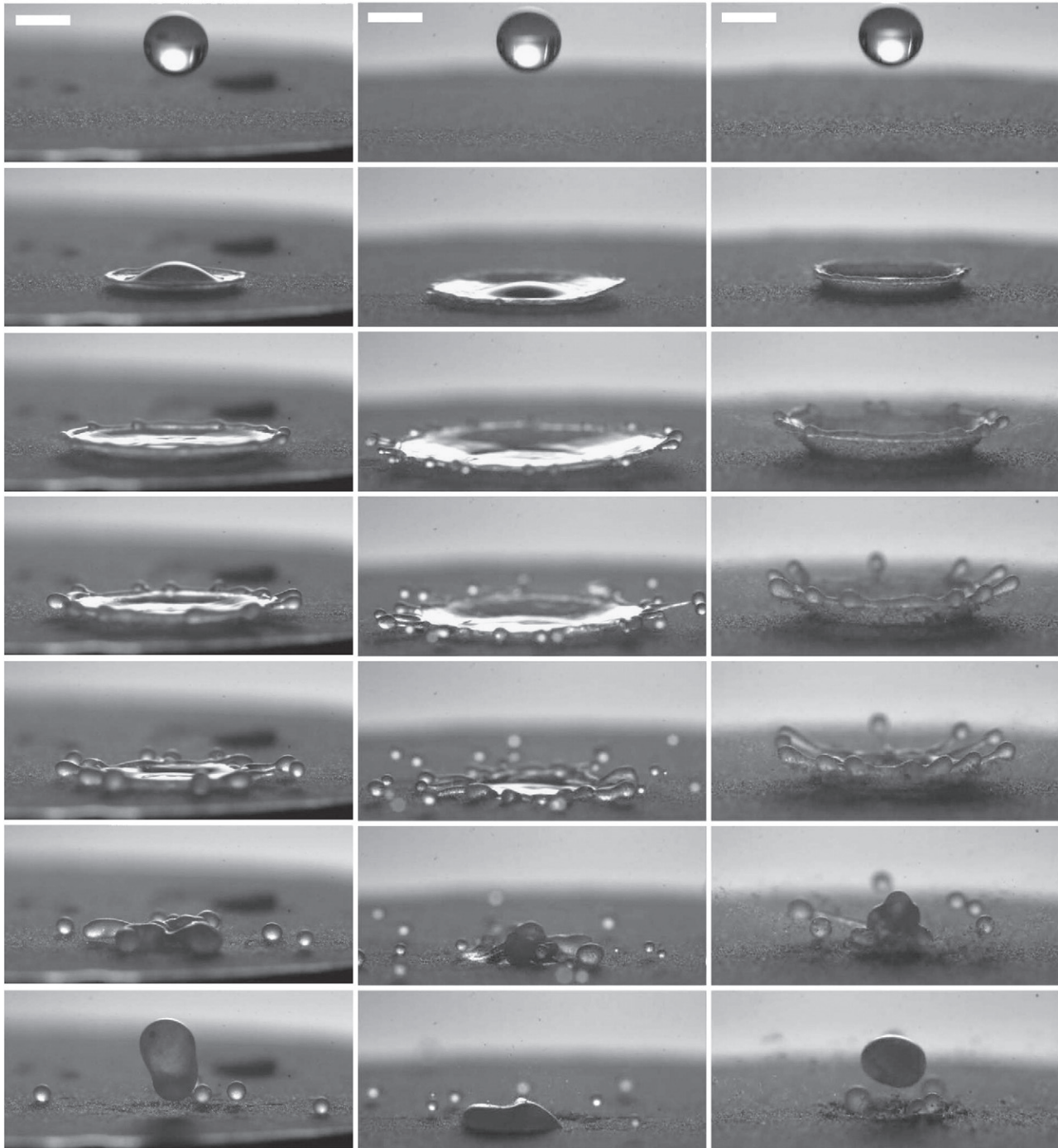


Fig. 11. Image sequences showing droplet breakage under different conditions for 50% glycerol drops ( $Bo = 0.92$ ,  $Oh = 0.019$ ). Frames shown are taken from the high-speed video sequences at  $-0.67$ ,  $0.67$ ,  $2$ ,  $3.33$ ,  $4.67$ ,  $7.33$  and  $17.33$  ms from impact. The impact conditions are (a)  $u_i = 2.56$  m/s,  $We = 257$ ,  $\phi = 0.58$ , (b)  $u_i = 3.24$  m/s,  $We = 411$ ,  $\phi = 0.58$  and (c)  $u_i = 3.24$  m/s,  $We = 411$ ,  $\phi \sim 0.57$  with additional surface scraping. The scale bars are 2 mm.

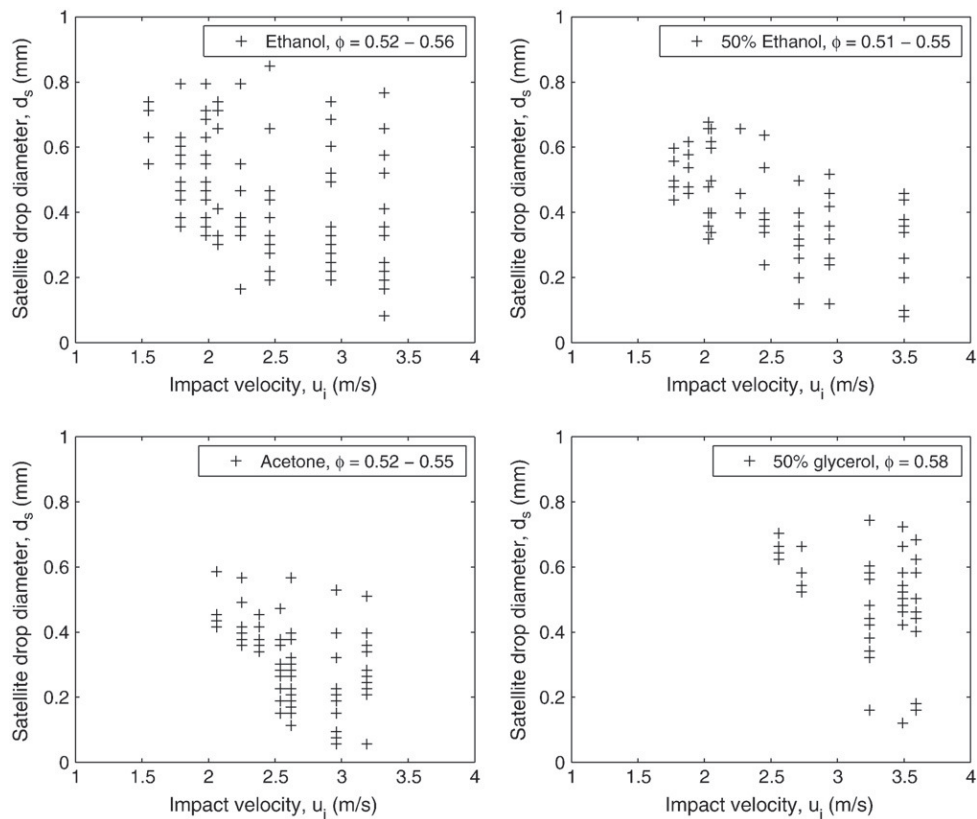


Fig. 12. Satellite drop diameters for ethanol, 50% ethanol, acetone and 50% glycerol plotted against drop impact velocity.

instability leads to droplet detachment (see Section 3.4). As such, the value  $d_{max}$  is measured to the base of the fingers. Below the fingering threshold,  $d_{max}/D$  increases in a linear fashion from 1.3 to 3.5 as  $u_i$  increases from 0.23 m/s to 1.9 m/s. Above the threshold, the spread diameters essentially become independent of the impact velocity with  $2.7 \leq d_{max}/D \leq 3.9$ . Fig. 6(b) shows representative images of acetone drops at  $d_{max}$  for low impact velocity ( $u_i = 0.27$  m/s), impact velocity just below the threshold ( $u_i = 1.78$  m/s) and impact velocity above the threshold ( $u_i = 2.43$  m/s).

Data for  $Bo \leq 1$  with  $0.51 \leq \phi \leq 0.55$  is shown in Fig. 7(a) where a notable discrepancy between the high-viscosity data for pure glycerol ( $\mu \sim 1000$  mPa s) versus low-viscosity data for water ( $\mu = 1$  mPa s) and 50% glycerol ( $\mu = 8.4$  mPa s) is observed. The fact that glycerol exhibits a much lower variation in  $d_{max}$  is due to the viscous dissipation of energy during impact. For water and 50% glycerol,

however, the deformation is clearly still dependent on the impact velocity, albeit weaker than for the lower surface tension drops in Fig. 6(a).

Select data for a range of packing fractions is shown in Fig. 7(b) for 50% glycerol drops. Only several data points (at low  $u_i$ ) for the lowest  $\phi$  could be obtained as the drop simply penetrates through the bed if the impact velocity is too high similar to the entry of a solid in loose powder beds [16,17]. From the data shown, the deformation appears to be rather insensitive to the packing fraction for  $u_i \lesssim 1.5$  m/s, but for higher impact velocities we generally see lower values of  $d_{max}$  for  $\phi = 0.51$  than for  $\phi = 0.57$ – $0.59$ .

Data from Figs. 6(a) and 7(a) are replotted against the impact Weber number in Fig. 8(a) and (b) respectively. Previous investigations of the maximum deformation of drops impacting solid surfaces have shown that the Weber number is the correct scaling parameter

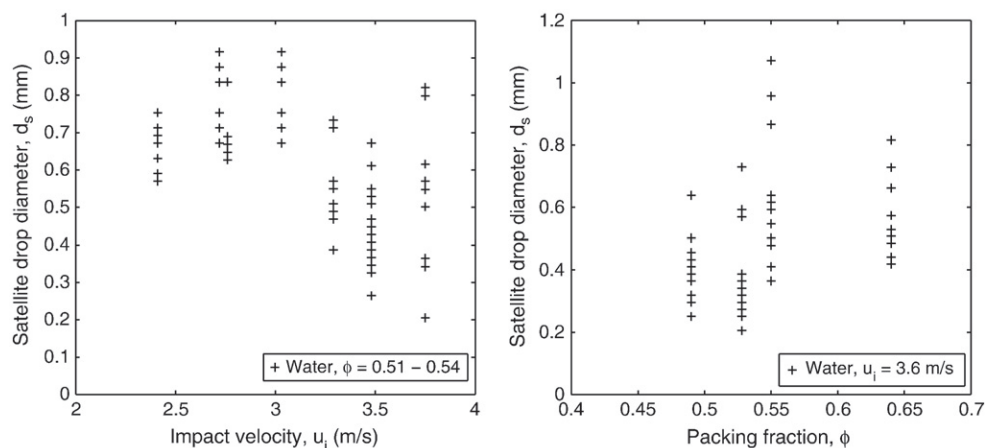


Fig. 13. Satellite drop diameters for water plotted against (a) impact velocity with  $0.51 \leq \phi \leq 0.54$  and (b)  $\phi$  with  $u_i = 3.6$  m/s.

where  $d_{max}/D \sim We^{1/4}$  for  $Bo > 1$  and  $d_{max}/D \sim We^{1/2}$  for negligible surface tension forces [12,13]. Both of these scalings, however, assume no energy dissipation through the target surface, which clearly becomes important for the case of a powder target surface; In our case, the powder bed itself provides a certain ‘cushioning’ effect for the drop so that the liquid does not experience such a strong deceleration as for a rigid solid surface. This effect, which is likely to be more pronounced for lower packing fractions (as seen in Fig. 7(b)) and higher density drops, is clearly observed in Figs. 8(a) and (b). In Fig. 8(a), for  $Bo > 1$ , the  $We^{1/4}$  scaling now provides an upper limit for the data which is more correctly described by the scaling  $d_{max}/D \sim We^{1/5}$  in over two orders of magnitude of the Weber number. In Fig. 8(b), the dependence on the Weber number is again reduced, by the arguments above, so that we can generally use  $d_{max}/D \leq We^{1/5}$  as an upper limit.

### 3.2. Retraction and rebound

After attaining  $d_{max}$ , the drops may either wet the powder and penetrate the beds (e.g. Fig. 3, right panel) or retract and rebound (e.g. Figs. 1 and 3, left panel). In the case of retraction, the shape of the drop may give rise to a singular jet (see Fig. 1 at  $t = 6.3$  ms) due to the collapse of the central apex cavity as reported for drops impacting a superhydrophobic solid [18]. The highest jet speeds observed herein are much lower than those previously reported [18] with the fastest jet occurring for the impact of 50% glycerol with  $u_i = 0.93$ ,  $\phi = 0.43$  and a resulting jet velocity  $v_{jet} \sim 6.8$  m/s. The occurrence of the jet is dependent on both the viscosity and the solids packing fraction in the bed. Essentially, if the liquid is too viscous to deform, an apex cavity will not be produced so jetting will not result. Likewise, if the packing is loose enough or the impact velocity too high, the drop will simply penetrate the bed. Here, we find that jets are observed for  $u_i < 2.2$  m/s,  $\mu \leq 8.4$  mPa s and  $\phi > 0.42$ . In such cases, as the jetting occurs during the rebound phase, we expect the jet emergence time to scale with  $\sqrt{\rho D^3 / \sigma}$ , so that the non-dimensional time,  $t_{jet} u_i / D \sim We^{1/2}$ . This scaling is plotted against experimental measurements in Fig. 9(a) where jetting was observed, showing good agreement.

At slightly later times, the drop may completely rebound from the powder surface. In drop impact studies onto rigid hydrophobic solids, rebound has been attributed to the weak adhesion between the liquid and the solid, as this is essentially what characterises a hydrophobic surface. In such circumstances, the time from impact to rebound (i.e. the contact time) has been found to be independent of the impact velocity [19]. In this study, when the liquid contacts the powder surface, the powder–liquid adhesion appears strong (evident from the powder coatings attained) and the rebound may benefit from the weaker inter-particle attractive forces. The contact time, however, exhibits a slight dependence on the impact velocity, shown in Fig. 9 (b). A plausible explanation for this apparent dependence is the added mass of the drop due to the powder adhesion/incorporation into the drop; as the impact velocity increases, the contact area increases so that more powder is added to the drop. As such, the effective mass of the drop increases which may slow down the rebound process. Based on the maximum spread diameters and original drop mass, we estimate that the mass increase during rebound is between 5% and 45% of the initial mass of the drop.

This effect naturally leads to a slightly poorer fit of the data in dimensionless form, shown in Fig. 9(c) for the normalised rebound times plotted against the Weber number.

### 3.3. Regime transitions

A summary of the different features observed is presented in Fig. 10 showing the phase diagram for the low viscosity liquids with  $0.51 \leq \phi \leq 0.55$  and in Table 3 for 50% glycerol at different packing fractions. The data points in Fig. 10 and entries in Table 3 represent the

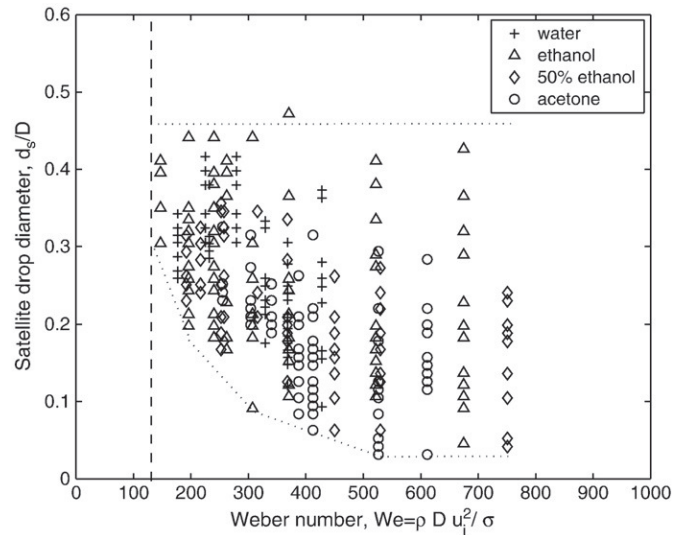


Fig. 14. Satellite drop diameters plotted against impact Weber number for low viscosity liquids.

onset of the feature observed where only the clear, common features identified are shown. The transitions plotted in the  $Oh-We$  plane show that the transitions occur over a relatively narrow range of  $We$  for water in this range of packing fractions, whereas the other, lower surface tension liquids exhibit a more diverse range of Weber numbers for the transitions. The different features observed for the different packing fractions in Table 3 also serve to highlight the strong influence of the powder in the impact dynamics. Maps of this type for a variety of drop sizes may help to characterise the origin of instabilities and non-uniformities in binder drop deposition.

### 3.4. Splashing – satellite drop generation

During the impact process, droplet breakage can occur due to the fingering instability which occurs at higher impact velocities thereby leading to a breakdown of the relationship between the wetted area of powder and impact velocity (see Fig. 6(a)). Fig. 11 shows some example sequences of the breakage of 50% glycerol drops for three different realisations. In each case, the overall packing fraction was kept very similar  $\phi = 0.58, 0.58$  and  $0.57$  respectively, whilst in the first trial (left panel) the impact velocity was  $u_i = 2.56$  m/s, in the



Fig. 15. Example of secondary nucleation from satellite drops produced following the impact of an ethanol drop with  $\phi \sim 0.4$ ,  $We = 410$ . The primary nucleus diameter is 2.3 mm, whilst the satellite drops produce secondary nuclei of diameters 685, 667, 611, 593 and 574  $\mu\text{m}$ . The scale bar is 5 mm.

second trial  $u_i = 3.24$  m/s and in the third trial  $u_i = 3.24$  m/s but the surface was artificially roughened with additional scraping. The outcomes of these different initial conditions are clear from the images, and analysis of the satellite drops shows that only 5 discrete drops in the range 620–700  $\mu\text{m}$  are generated from the first trial, approximately 25 drops in the range 160–740  $\mu\text{m}$  are generated for the second trial, whilst the third trial only generates 5 drops in the range 620–760  $\mu\text{m}$ . Note also the higher crown angle in the third column for the low packing fraction. This demonstrates that both impact velocity and the bed surface strongly influence the breakage of the impacting drop and the generation of satellite droplets.

Figs. 12 and 13 show the full analysis of the satellite drop sizes generated for a range of impact velocities and liquids. In Fig. 12, for ethanol, 50% ethanol and acetone, the packing fraction varied slightly between trials, but did not appear to significantly influence the qualitative trends over the ranges used. For 50% glycerol, the packing fraction was fixed at  $\phi = 0.58$ . In Fig. 13, we plot the satellite drop sizes for (a) varying impact velocity for similar  $\phi = 0.51$ –0.54 and (b) varying packing fraction for fixed impact velocity of  $u_i = 3.6$  m/s.

Despite considerable scatter in the data, some general features can clearly be seen; firstly, the number of drops increases as the impact velocity is increased. This is generally to be expected as the number of fingers,  $N_f$ , increases with impact velocity, or more precisely with an impact Reynolds number defined by Marmanis and Thoroddsen [20] as  $N_f \propto Re_I = u_i(\pi^2 \rho D^3 / 16\sigma)^{1/4} / \nu^{1/2}$ . The number of fingers does not necessarily dictate the final number of drops due to coalescence of drops and merging of fingers [1] but shows that we should expect to see more satellite drops as  $u_i$  increases. Secondly, the size of the first satellite drops produced from the tips of the fingers decreases, this can be understood by considering the increase in  $N_f$  as well as the thinning of the liquid ejecta sheet as  $u_i$  increases due to conservation of mass. As such, the overall drop size distribution widens as  $u_i$  increase, which is seen in the data. The scaling of Marmanis and Thoroddsen [20] also suggests that the number of drops should decrease with increasing surface tension and/or viscosity for a given impact velocity, which can also be seen in Figs. 12 and 13.

An exact quantitative description of the satellite drop generation is complicated by the inherent roughness of the target surface [1] and the

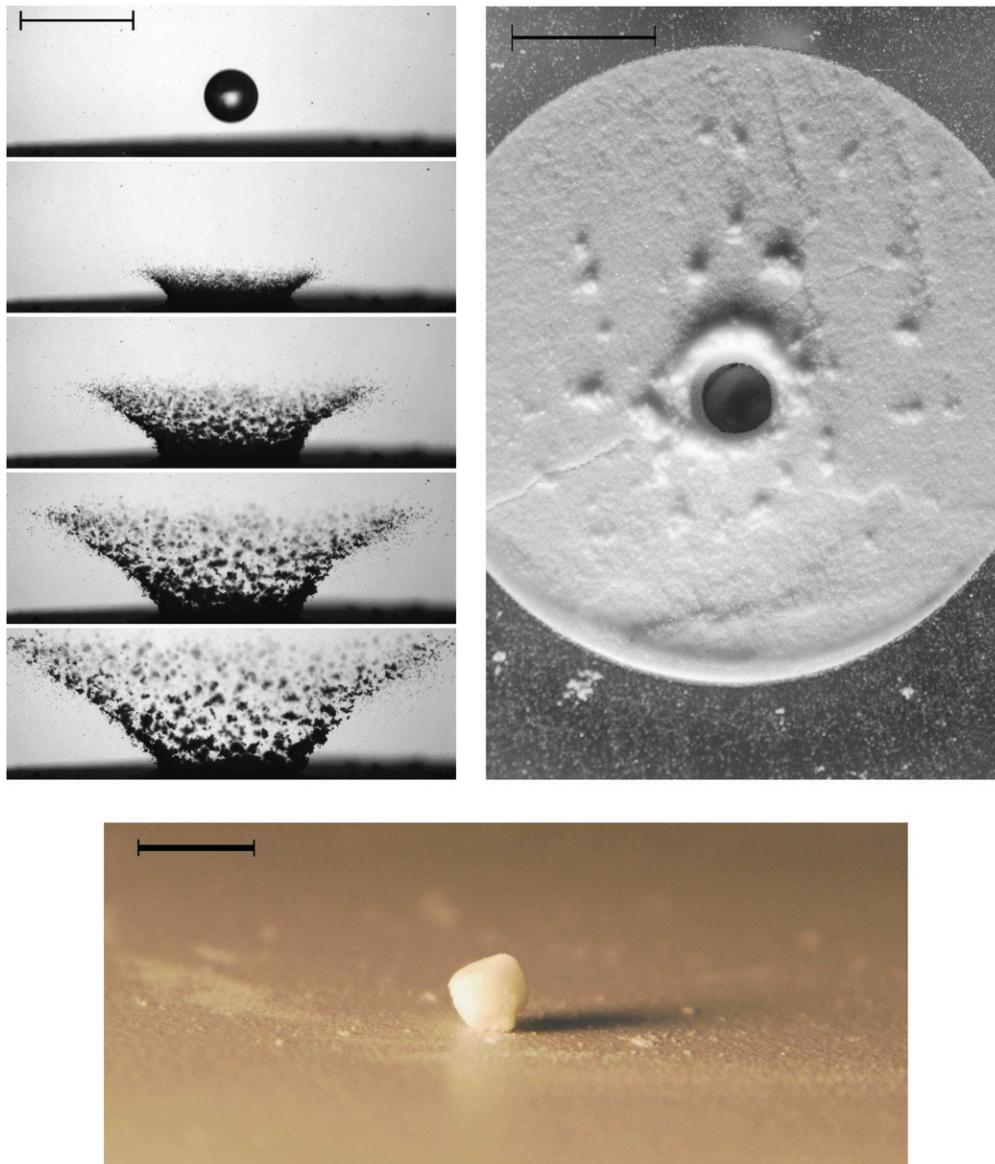


**Fig. 16.** Top image, left panel: Frames shown are taken from a high-speed video sequence at  $-0.67, 2.67, 5.33, 8, 10.67$  and  $13.33$  ms from the impact of a  $D = 2.4$  mm 50% glycerol drop. The impact conditions are  $\phi \sim 0.41$ ,  $We = 188$ ,  $Oh = 0.019$ . Top image, right panel: Final view of the surface several seconds after impact. Bottom image: Granule nucleus structure after removal from the loose particle bed. Scale bars are 5 (top left, bottom) and 10 (top right) mm respectively.

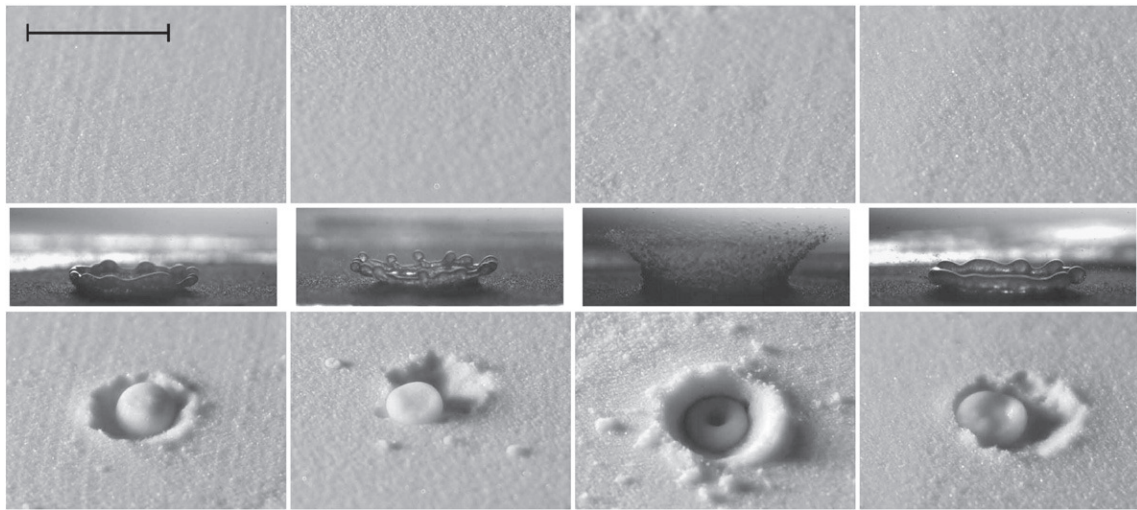


**Fig. 17.** Before (top row), during (middle row) and after (bottom row) images of the surface for impacts of acetone (first column), ethanol (second column) and water (third and fourth columns). Frames shown in the middle row are taken from the high-speed video sequence at 4 ms from impact. The impact conditions, from left to right, are  $\phi \sim 0.4$ ,  $We = 416$ ;  $\phi \sim 0.4$ ,  $We = 410$ ;  $\phi \sim 0.39$ ,  $We = 208$ ;  $\phi \sim 0.43$ ,  $We = 216$ . The scale bar is 5 mm.

possibility of powder becoming incorporated into the liquid sheet during expansion. This will inevitably alter the break-up and recoil of the fingers.

In Fig. 14, data for the low viscosity liquids is plotted against the Weber number where the satellite drop diameters are normalised with respect to the impact drop diameter. From this plot we see that no drops are generated for  $We \leq 140$ , indicated by the vertical dashed line. At the onset of fingering and satellite drop generation, the minimum drop size gradually decreases from approximately  $0.3D$  for  $We \sim 140$  to approximately  $0.03D$  for  $We > 500$ . The maximum satellite drop size also generally decreases, except for ethanol which maintains a maximum drop size of approximately  $0.45D$  throughout the range of Weber numbers tested here.

The breakage of impacting drops and generation of satellite droplets can have significant consequences for the granule nuclei size distributions as the impact of satellite drops themselves can serve as secondary nucleation sites. An example of this is shown in Fig. 15 following the impact of an ethanol drop where the primary nucleus (from the impacting drop) has a diameter of 2.3 mm whilst the secondary nuclei have diameters 574–685  $\mu\text{m}$ . Note that the packing fraction here,  $\phi \sim 0.4$ , is much lower than those considered above in Figs. 12–14, but clearly illustrates the significance of this phenomena.

### 3.5. Nucleation – loose packings

Fig. 16 shows the powder ejecta following the impact of a 50% glycerol drop onto a loose bed ( $\phi = 0.41$ ). This ejecta is similar to that observed following the entry of a solid into a loose powder bed [16]. The drop penetrates several millimeters into the bed, without rebounding, where nucleation will commence. In this case the nucleation mechanism is immersion, whereby the small base particles are immersed in the large impacting drop. The final view of the powder target is shown in right panel of Fig. 16 where dry clumps of the ejected powder can be seen, whilst the bottom image in Fig. 16 shows the saturated granule nucleus after removal from the bed. The resulting granule diameter is approximately 2.3 mm (the approximation given due to its asymmetry).

Further examples of the granule nuclei formations are shown in Fig. 17. In this figure, images of the powder surface before, during and after impact are shown for acetone, ethanol and water all for  $u_i = 2.35$  m/s. The after shots in the final row were taken approximately 30 s after impact so that no further evolution of the nuclei is seen. Again we can identify, as expected, the nucleation mechanism as immersion as the impacting drops are two orders of magnitude larger than the base particles. By inspection, the granule nuclei indeed

appear saturated. The final nuclei diameters are  $d_g \sim 2.6, 2.3, 2.8$  and 2.9 mm respectively. Note that the clumps seen in the third column, for water onto a low packing fraction bed, are simply clusters of dry powder, not secondary nuclei as seen for the ethanol drop (second column). The two cases for water, shown in the third and fourth columns, highlight the influence of the packing fraction not only on the impact dynamics (middle row) but also on the final appearance of the granule nucleus; The structure for the low packing fraction of  $\phi = 0.39$  has formed a toroidal shape, where the top of the granule has sunk-in which has been observed previously for loose packings [3]. Hapgood et al. [3] assert that this granule form may arise due to internal voidage in the granule itself.

A close-up of the toroidal granule structure is shown in Fig. 18 following the impact of an ethanol drop onto a loose bed with  $\phi = 0.39$ , clearly showing the collapse of the central region of the granule, again indicating that the granule may have attained internal voidage during nucleation.

A qualitative comparison of the wetting and nucleation for the viscous drops is shown for  $\mu = 8.4$  mPa s with  $\phi = 0.45$  in Fig. 19 and  $\mu = 1000$  mPa s with  $\phi = 0.52$  in Fig. 20 for similar impact velocities. In Fig. 19, for the looser packing, the drop generates a crater in which the drop sits until nucleation by immersion occurs, whereas for the high-viscosity drop onto a denser packing, the liquid spreads and penetrates the powder to form a nucleation site.

A summary of the qualitative features observed in this section is quantified in Fig. 21, where we plot data only where measurements

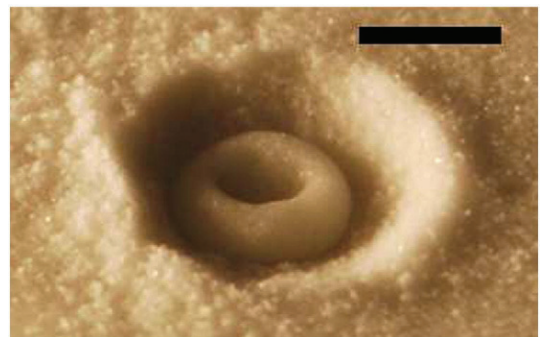


**Fig. 18.** Close-up of a granule nucleus formation following the impact of a  $D = 1.8$  mm ethanol drop onto a loose powder bed  $\phi = 0.39$  with  $u_i = 2.3$  m/s ( $We = 324$ ). The scale bar is 2 mm.

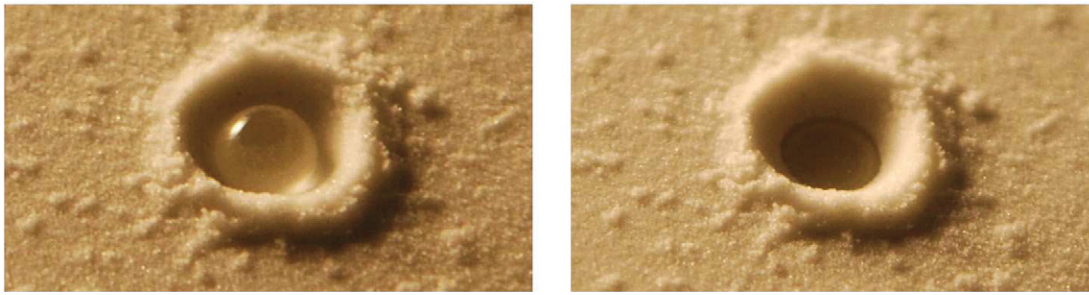


**Fig. 19.** Snapshots of a 50% glycerol drop before and after drainage. The impact conditions are  $\phi = 0.45$ ,  $We = 68$ ,  $Bo = 0.92$ ,  $Oh = 0.02$ . The time interval between images is several seconds.

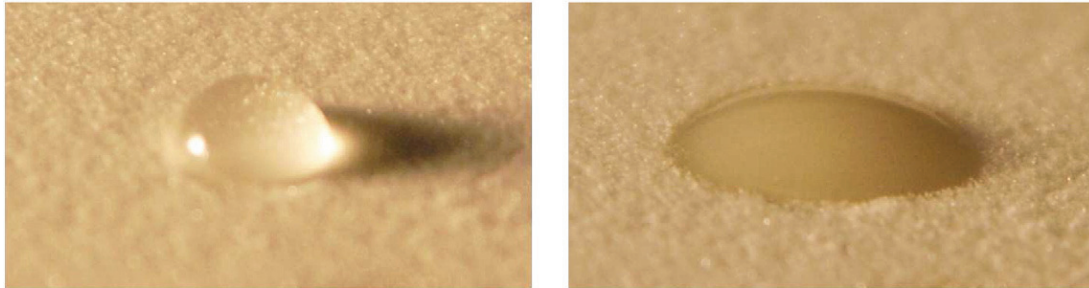


**Fig. 20.** Snapshots of a pure glycerol drop before and during drainage. The impact conditions are  $\phi = 0.52$ ,  $We = 50$ ,  $Bo = 1$ ,  $Oh = 2.3$ . The time interval between images is several seconds.

could be made (for example granule nuclei diameters could only be measured accurately when clearly visible). The data indicates that the size of the granule nucleus appears rather insensitive to the impact velocity over the range of  $\phi$  and  $u_i$  tested here. All measurements for the granule nuclei diameters are in the range  $2.3 \text{ mm} \leq d_g \leq 3 \text{ mm}$ . Instead, it appears  $d_g$  is more dependent on the initial drop diameter; this also applies to secondary nuclei formed from satellite drops (see Fig. 15).

In contrast, the crater diameter increases from  $d_c = 3.4 \text{ mm}$  for  $u_i = 0.75 \text{ m/s}$  to  $d_c = 6 \text{ mm}$  for  $u_i = 3.55 \text{ m/s}$ . Following previous observations of impact cratering by a solid sphere [21], this parameter is expected to scale with  $u_i^{0.46}$ , which is shown on the plot by the

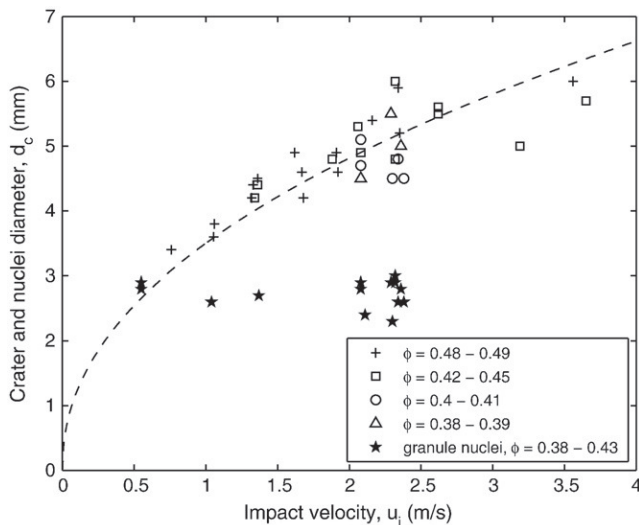


**Fig. 21.** Crater and granule nuclei diameters for a variety of low packing fractions ( $0.38 \leq \phi \leq 0.49$ ) as a function of impact velocity. The dashed line shows the scaling  $u_i^{0.46}$ .

dashed line (where a numerical prefactor of 3.5 found from regression includes the influence of the mass of the drops). This scaling shows reasonable agreement, with a certain amount of scatter for various packing fractions.

#### 3.5.1. Anomalous features – pinning

Some interesting observations were made for realisations with higher packing fractions ( $\phi > 0.5$ ) and relatively low impact velocities, where instead of full drop rebound, some section(s) of the base contact area become pinned. In some cases, such as that shown in Fig. 22 for a 50% glycerol drop, the entire base becomes pinned leading to pinch-off of a drop at the apex of the liquid structure. Note that the pinch-off occurs at the demarcation of the surface powder coating, so that the secondary drop has a ‘clean’ surface whereas the cone base is coated with powder. The drop subsequently falls and coalesces with the base. This pinned rebound indicates that only a small amount of liquid penetration takes place during this time. This is validated by estimating the volume of liquid in the cone and secondary drop which, for this instance constitutes approximately 97% of the liquid volume of the impacting drop. It is this small penetration of liquid into the top layers of the powder that gives rise to the pinned base.

In other cases, only a section of the base is pinned, such as those shown in Fig. 23 for 50% glycerol at a lower impact velocity and Fig. 24 for ethanol onto a looser packing.

We believe this ‘pinned rebound’ feature is due to partial liquid penetration into the inherent heterogeneous void structure in the powder bed.

## 4. Conclusions

An experimental study into the initial dynamics of drop impact onto powder surfaces has been performed. By focusing on a single base particle size distribution and drop sizes with  $Bo \sim 1$ , we performed a systematic study of the effects of the initial bed packing fraction and the physical properties of the impacting drop. The qualitative features of this phenomenon have been shown to depend

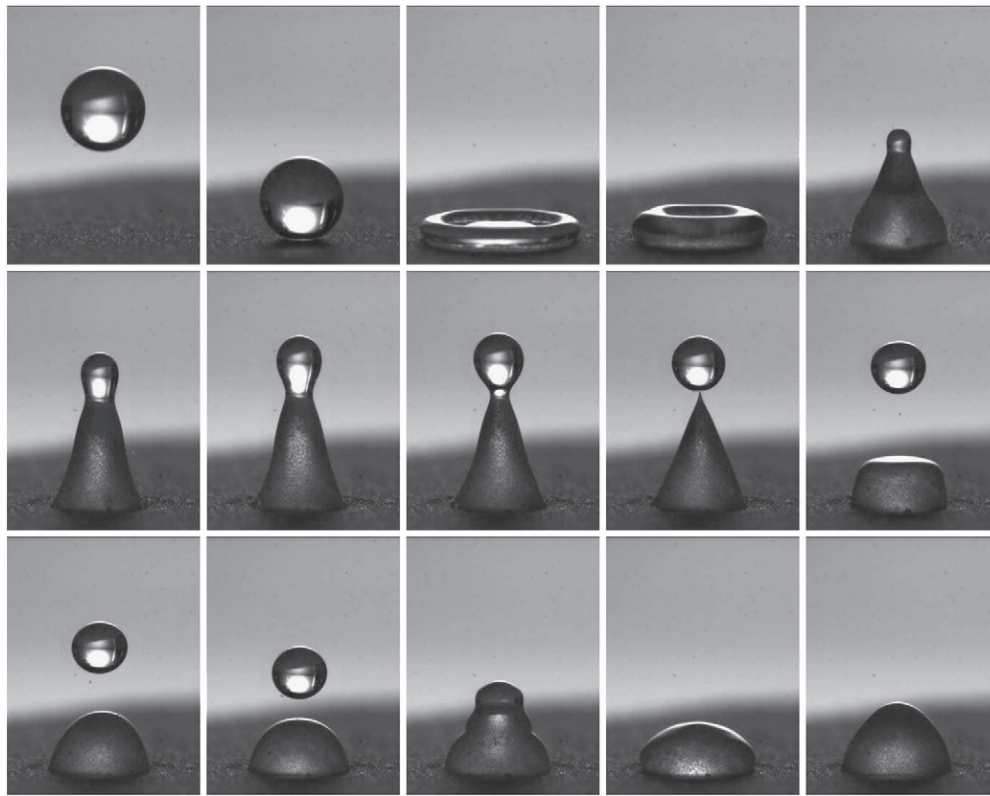


**Fig. 22.** Images showing the formation of a cone structure due to pinning at the base of a 2.4 mm 50% glycerol drop. Frames shown are taken at –2.7, 0, 2.7, 5.3, 8, 10.7, 13.3, 16, 18.1, 20.8, 26.1, 31.5, 38.1, 43.5 and 48.8 ms from impact. The impact conditions are  $u_i = 0.96$  m/s,  $We = 36$ ,  $Oh = 0.019$ ,  $\phi \sim 0.587$ .

strongly on the bed packing fraction,  $\phi$ , the impact Weber number,  $We$ , as well as the Ohnesorge number,  $Oh$ , characterising the role of viscosity and the Bond number,  $Bo$ . By varying these important parameters, a range of characteristic behaviours were observed from spreading and retraction leading to full rebound to prompt splashing and powder ejection.

The spreading dynamics were found to exhibit some similarity to impact onto a hydrophobic surface. For drops with  $Bo > 1$  we found that the maximum spread of the drops scales with  $We^{1/5}$  whereas for viscous drops with  $Bo < 1$  this scaling provided the upper limit due to the increased cushioning effect of the powder bed and the additional loss of kinetic energy due to particle attachment and entrainment. The

time from impact to rebound was found to increase slightly with impact velocity due to the effects of the added mass.

Above a threshold Weber number, the impacting drops generate satellite droplets and we find that the total number of satellites and size ranges increase with the impact Weber number. These satellite drops were also shown to serve as secondary nucleation sites. Examples of nucleation are shown and we find the mechanism of immersion appears to be insensitive to the impact velocity in terms of the final granule nucleus diameter.

The influence of the impact conditions coupled with powder wettability on the features observed herein and penetration times is the subject of on-going studies.



**Fig. 23.** Images showing the pinning at the base of a 2.1 mm 50% glycerol drop. Frames shown are taken at 0, 3.5, 7.1, 12.7, 20.5, 45.8 ms from impact. The impact conditions are  $u_i = 0.7$  m/s,  $We = 16.8$ ,  $Oh = 0.019$ ,  $\phi \sim 0.55$ . The scale bar is 2 mm.



**Fig. 24.** Images showing the pinning at the base of a 1.8 mm ethanol drop. Frames shown are taken at 0, 3.4, 7.3, 13.3, 21, 38 ms from impact. The impact conditions are  $u_i = 0.84$  m/s,  $We = 43$ ,  $Oh = 0.0066$ ,  $\phi \sim 0.52$ . The scale bar is 2 mm.

## Acknowledgments

This work was supported by the Science and Engineering Research Council of A\*STAR (Agency for Science, Technology and Research), Singapore. The authors would like to thank Ng Junwei for assistance in measurements of the powder size distribution and liquid viscosities.

## References

- [1] A.L. Yarin, Drop impact dynamics: splashing, spreading, receding, bouncing, *Annu. Rev. Fluid Mech.* 38 (2006) 159–192.
- [2] K.P. Hapgood, J.D. Lister, R. Smith, Nucleation regime map for liquid bound granules, *AIChE J.* 49 (2003) 350–361.
- [3] K.P. Hapgood, S.M. Iveson, J.D. Lister, L.X. Liu, in: A.D. Salman, M.J. Hounslow, J.P.K. Seville (Eds.), *Handbook of Powder Technology*, 11, Elsevier B.V., 2007, pp. 897–977.
- [4] K.P. Hapgood, J.D. Lister, S.R. Biggs, T. Howes, Drop penetration into porous powder beds, *J. Colloid & Interface Sci.* 253 (2002) 353–366.
- [5] M. Denusek, G.L. Smith, B.J.J. Zelinski, N.J. Kreidl, D.R. Uhlmann, Capillary penetration of liquid droplets into porous materials, *J. Colloid & Interface Sci.* 158 (1993) 114–120.
- [6] V. Chouk, G. Reynolds, M. Hounslow, A. Salman, Single drop behaviour in a high shear granulator, *Powder Tech.* 189 (2) (2009) 357–364.
- [7] K.P. Hapgood, T.H. Ngyuen, S. Hauw, S. Iveson, W. Shen, Rewetting effects and droplet motion on partially wetted powder surfaces, *AIChE J.* 55 (6) (2009) 1402–1415.
- [8] K.P. Hapgood, B. Khanmohammadi, Granulation of hydrophobic powders, *Powder Tech.* 189 (2) (2008) 253–262.
- [9] L. Forny, I. Pezron, K. Saleh, P. Guigon, L. Komunjer, Storing water in powder form by self-assembling hydrophobic silica nanoparticles, *Powder Tech.* 171 (2007) 15–24.
- [10] N. Estiaghi, J.J.S. Liu, K.P. Hapgood, Formation of hollow granules from liquid marbles: small scale experiments, *Powder Tech.* 197 (2010) 184–195.
- [11] P. Aussillous, D. Quere, Properties of liquid marbles, *Proc. R. Soc. A* 462 (2006) 973–999.
- [12] Y. Renardy, S. Popinet, L. Duchemin, M. Renardy, S. Zaleski, C. Josserand, M.A. Drumright-Clarke, D. Richard, C. Clanet, D. Quere, Pyramidal and toroidal water drops after impact on a solid surface, *J. Fluid Mech.* (2003) 69–83.
- [13] C. Clanet, C. Beguin, D. Richard, D. Quere, Maximal deformation of an impacting drop, *J. Fluid Mech.* 517 (2004) 199–208.
- [14] D. Bartolo, C. Josserand, D. Bonn, Retraction dynamics of aqueous drop upon impact on non-wetting surfaces, *J. Fluid Mech.* 545 (2005) 329–338.
- [15] J.C. Bird, S. Madre, H. Stone, Short-time dynamics of partial wetting, *Phys. Rev. Lett.* 100 (2008) 234501.
- [16] J.O. Marston, J.P.K. Seville, Y.-V. Cheun, A. Ingram, S.P. Decent, M.J.H. Simmons, Effect of packing fraction on granular jetting from solid sphere entry into aerated and fluidized beds, *Phys. Fluids* 20 (2008) 023301.
- [17] S.T. Thoroddsen, A.Q. Shen, Granular Jets *Phys. Fluids* 13 (2001) 4.
- [18] D. Bartolo, C. Josserand, D. Bonn, Singular jets and bubbles in drop impact, *Phys. Rev. Lett.* 96 (2006) 124501.
- [19] D. Richard, C. Clanet, D. Quere, Contact time of a bouncing drop, *Nature* 417 (2002) 811.
- [20] H. Marmanis, S.T. Thoroddsen, Scaling of the fingering pattern of an impacting drop, *Phys. Fluids* 8 (6) (1996) 1344–1346.
- [21] S.J. de Vet, J.R. de Bruyn, Shape of impact craters in granular media, *Phys. Rev. E* 76 (2007) 041306.